Electronic Supplementary Material (ESI) for Materials Horizons.

Hierarchical self-assembly of bulk metamaterials enables isotropic magnetic permeability parameter at optical frequencies.

*Sergio Gomez-Graña[a], Aurélie Le Beulze[a], Mona Treguer-Delapierre[a], Stéphane Mornet[a], Etienne Duguet[a], Eftychia Grana[b], Eric Cloutet[b], Georges Hadziioannou[b], Jacques Leng[c], Jean-Baptiste Salmon[c], Vasyl G. Kravets[d], Alexander N. Grigorenko[d], Naga Anirudh Peyyety[e], Virginie Ponsinet[e], Philippe Richetti[e], Alexandre Baron[e], Daniel Torrent[e], Philippe Barois[e]**

[a] University of Bordeaux, CNRS, ICMCB, UPR 9048, 33600 Pessac, France.

[b] University of Bordeaux, CNRS, LCPO, UMR 5629, 33615 Pessac, France.

[c] University of Bordeaux, CNRS, Solvay, LOF, UMR 5258, 33608 Pessac, France.

[d] School of Physics and Astronomy, University of Manchester, Manchester, M13 9PL, UK.

[e] University of Bordeaux, CNRS, CRPP, UPR 8641, 33600 Pessac, France.

* e-mail: barois@crpp-bordeaux.cnrs.fr

Supplementary information

Note: additional references cited this section are denoted by ^{Sx}.

1 – Synthesis of meta-molecules: Experimental section

Chemicals: Silver nitrate (AgNO3, 99.999%), sodium hydrosulfide (NaHS), L-arginine (≥ 98%), tetraethyl orthosilicate (TEOS; ≥ 90%), sodium citrate dihydrate (≥ 99%), cyclohexane (> 99.7%), poly-(vinyl-pyrrolidone) (PVP; Mw~55,000) and Acetone (CH_3COCH_3, ≥99.5%) were purchased from Sigma-Aldrich. Iodomethane (CH_3I, 99%) was purchased from Acros Organics and N,N-Dimethylformamide (DMF, anhydrous 99.8% packaged under Argon in resealable bottle) from Alfa Aesar. Ethylene glycol (EG, 99%), ammonium hydroxide (NH_4OH, 28-30 wt.%) were obtained from J.T. Baker. Absolute ethanol was purchased from Atlantic Labo. Poly(1-vinyl-1,2,4-triazole) (PVTri, MW=21,260 g/mol calculated through conversion from ^{1}H-NMR) was prepared through Reversible Addition Fragmentation Chain Transfer (RAFT) polymerization at 60°C in DMF [S1].

Synthesis:

Cationic polymer electrolyte: Poly(1-vinyl-4-methyl-1,2,4-triazolium iodide) ($PVMeTri^+I^-$) was synthesized through quaternization of the corresponding neutral polymer [S2]. 400 mg of PVTri (4.2 mmol) is refluxed under inert atmosphere with a large excess (1 mL, 16 mmol) of CH_3I in DMF (10% w/v). Final product is recovered by precipitation in 250 mL acetone and then is dried at 40°C for 20h (726 mg, yield 72.7%, 82.7% quaternized product calculated from ^{1}H-NMR data, see Fig. S1). ^{1}H NMR (400.1 MHz, NS=16, DMSO-d6) δ (ppm): 10.4-8.8 (2H, cationic polymer ring), 8.7-7.5 (2H, neutral polymer ring), 4.8-4.1 (1H, cationic polyelectrolyte chain), 4.1-3.5 (1H, neutral polymer chain / 3H, CH_3 cationic polymer), 2.5-1.8 (2H, polymer chain both neutral and cationic).

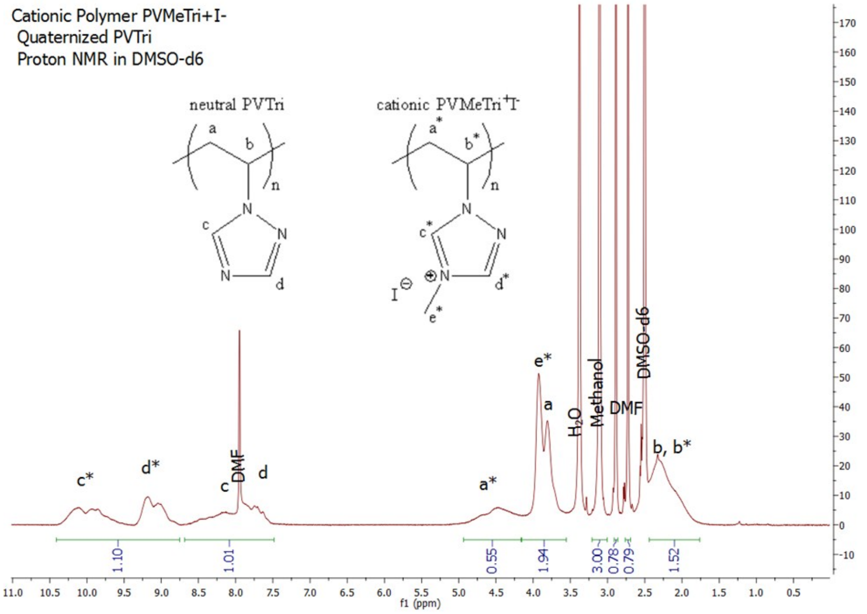

Figure S1: *^{1}H-NMR spectrum for the cationic polymer electrolyte. NMR measurements were carried out at 298 K on a Bruker Avance spectrometer operating at 400.1 MHz with NS=16. The relaxation time was set at 2s and DMSO-d6 was used as an internal reference (δ=2.50 ppm).*

<u>Silver nanoparticles:</u> Silver nanospheres were synthetized following to the procedure of Massé *et al*. [S3] In two different vials, 16.9 mg of NaHS were dissolved in 10 mL of EG and 900 mg of PVP in 30 mL of EG. Both solutions were left to age for 4 h under magnetic stirring. After 1h 30 min, 120 mL of EG was introduced in a rounded flask, being equipped with a reflux condenser and the temperature was increased to 150°C. An Argon flux was introduced in the rounded flask with the EG for the last 30 minutes in order to create an inert atmosphere. After 4 hours of aging, 70 µL of the NaHS solution and 30 mL of the PVP solution were added. Immediately after, 10 mL of EG solution containing 240 mg of silver nitrate was added to the rounded flask. After 10 min, the reaction was quenched introducing the rounded-beaker in an ice-bath and adding 50 mL of cold absolute ethanol. Finally, the silver nanoparticles were washed 3 times by using a Millipore Stirred Ultrafiltration Cell with a regenerated cellulose membrane (100 kDa). Then the nanoparticles were concentrated to ~10 mL by using the ultrafiltration technique.

<u>Silica nanoparticles:</u> 345 mL of an aqueous solution of L-arginine (7.5 mM) and 22.5 mL of cyclohexane were introduced in a 500-mL rounded beaker equipped with a magnetic stirrer and the resulting biphasic liquid was heated at 60°C. Then, 37.5 mL of TEOS were added to the top organic phase. The stirring speed was modified in order to form an interface with a constant area between both phases. After 24h, the cyclohexane was removed in a rotary evaporapor at 50°C. A further growth of the silica nanoparticles until 100nm was performed using the Stöber method: 50 mL of ethanol, 5 mL of NH4OH (1 M), and 5 mL of the aqueous suspension of silica seeds were mixed in a 150-mL round-beaker. A pre-determined volume of TEOS diluted in 20 mL of absolute ethanol was added at a rate of 1 mL/h by an automatic syringe pump.

<u>Layer-by-Layer (LbL) adsorption on silica nanospheres:</u> The LbL technique was applied according to a previously reported protocol [21]. Firstly, the silica nanoparticles were washed 3 times by centrifugation at 9000 g for 10 min, the pellet was redispersed in ultrapure water. 10 mL of the silica nanoparticles were added to 20 mL of a solution of cationic polymer (2 mg/mL). The

adsorption of the polymer onto the silica nanospheres was allowed to proceed for 30 min in a roller mixer. The excess of cationic polymer was removed by centrifugation at 6,000 g for 10 min, the pellet was redispersed in 10 mL of water.

Synthesis of Raspberry-like nanoclusters: Typically, 990 µL of water was mixed with 10 µL of the polyelectrolyte-modified silica beads, adding the solution drop-wise in 9 mL of washed silver nanoparticles solution. The mixture was allowed to stir overnight at room temperature and protected from light exposure to avoid the silver oxidation. The excess of metallic nanoparticles was eliminated by centrifugation at 1500 g during 10 min, the pellet with the nanoclusters was redispersed in 1 mL of water. A silica shell was further added in order to keep the raspberry shape. Such silica shell was done by adding 10 mL of ethanol, 250 µL of ammonium hydroxide and 1 µL of TEOS to the solution. The reaction was kept overnight and a centrifugation was performed to remove the free silica nuclei in excess. A further concentration of the sample was performed to obtain a concentrated sample (40 µL at volume fraction of order 1%) for the microfluidics assemblies.

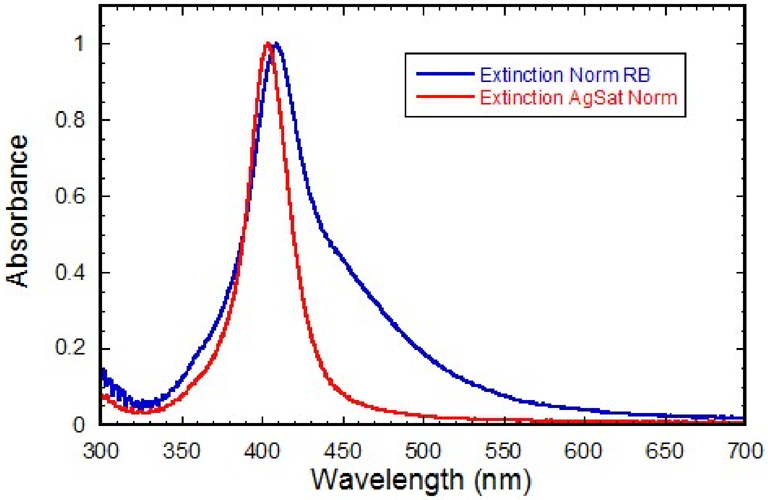

Figure S2: *Extinction spectra of a suspension of Ag satellites (red) and MNCs (blue).*

2 – Microfluidic assembly:

Microfluidic evaporation cells were created using standard soft photolithography techniques. A master template defining the micro-channels was first made with a photocurable resist polymer. A polydimethylsiloxane (PDMS) thin membrane (e ≈ 30 µm) was prepared by spin coating a PDMS solution onto the master template followed by curing at 60°C. At the same time, a thick PDMS stamp was done by curing the PDMS in a Petri dish at 60°C. Using plasma activation, the PDMS stamp was pasted on the PDMS membrane at one end of the micro-channels. The membrane was then peeled off from the template and punched to create an opening for the reservoir. The PDMS microfluidic chip was deposited on a microscope slide, allowing the evaporation of the solvent only through the membrane.

The MNCs dispersion was introduced in the reservoir, and the channels filled up with the MNCs solution. Due to the evaporation of the water through the PDMS membrane the MNCs accumulate at the dead end of the channel, hence forming the 3D material replicating the channel shape and size. When the reservoir is completely empty, the PDMS membrane is peeled off the glass substrate, leaving the metamaterial on the glass slide.

3 – Imaging:

Transmission electron microscopy (TEM) images were obtained with a JEOL JEM 1400 transmission electron microscope operating at an acceleration voltage of 120 kV. Scanning electron microscopy (SEM) images of assembled 3D metamaterial have been obtained using a JEOL JSM-6700F FEG scanning electron microscope operating at an acceleration voltage of 15.0 kV for secondary-electron imaging (SEI).

4 – Light scattering experiment:

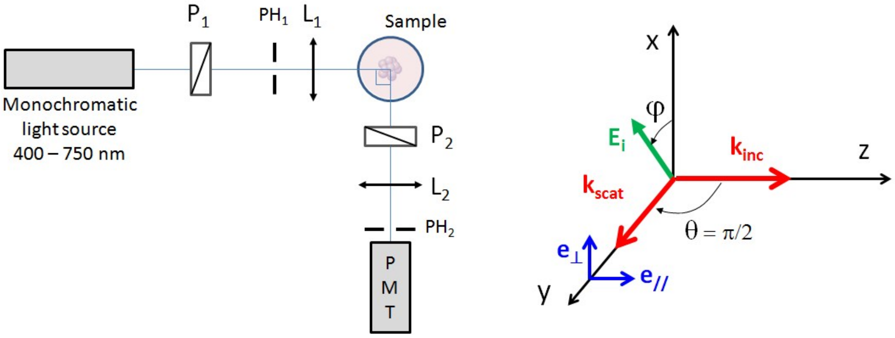

Figure S3: *Schematic view of the light scattering setup (left) and scattering geometry (right). The rotation of the input polarizer P_1 controls the incident polarization angle φ. The output polarizer P_2 enables to collect the scattering along the transverse ($\mathbf{e}_\perp$) and axial ($\mathbf{e}_{//}$) directions. PH1 and PH2 are pinholes, L1 and L2 focusing lenses.*

A supercontinuum white source (SuperK EXB-6 with SuperK Varia monochromator from NKT Photonics) was used to deliver a monochromatic light beam. The adjustable bandwidth was set to 6 nm. The linear polarization of the incident light was set by a Glan-Taylor polarizer (Thorlabs GL5-A) mounted on a rotation stage to rotate the incident polarization by an angle φ. The residual polarization of the source produced a weak variation of the irradiance of order +/- 4% upon rotation φ which was corrected in data analysis. The scattered light was collected with a photomultiplier tube (PMT Hamamatsu H10682-01) coupled with a photon counting unit (Hamamatsu C8855-01) at a fixed scattering angle $\theta = 90°$. The polarization of the scattered light was analyzed by a second Glan-Taylor polarizer (Thorlabs GL10-A) set perpendicular or parallel to the scattering plane to collect the $I_{\perp S}$ and $I_{//S}$ signal respectively.

The intensities $I_{\perp S}$ and $I_{//S}$ measured along the two output polarizations read:

$$I_{\perp S}(\varphi) = I_0(\lambda)\frac{N_{MNC}}{k^2}\left|S_1(\theta = 90°)\right|^2 \delta\Omega\ T(\lambda)\ g(\lambda,\delta\Omega)\times\sin^2\varphi = A_\perp(\lambda)\sin^2\varphi \qquad \text{(S1a)}$$

$$I_{//S}(\varphi) = I_0(\lambda)\frac{N_{MNC}}{k^2}\left|S_2(\theta = 90°)\right|^2 \delta\Omega\ T(\lambda)g(\lambda,\delta\Omega)\times\cos^2\varphi = A_{//}(\lambda)\cos^2\varphi \qquad \text{(S1b)}$$

in which $I_0(\lambda)$ is the spectral irradiance of the incident beam, N_{MNC} is the number of MNC scatterers in the scattering volume, $\delta\Omega$ is the solid angle of the detection window. $g(\lambda,\delta\Omega)$ is an unknown function that accounts for the spectral sensitivity of the detector and optical transmission or reflection of all optical elements. The spectral transmission $T(\lambda)$ account for the absorbance of the suspension.

The $I_{\perp S}$ and $I_{//S}$ signals are shown in inset of Fig. S4 versus the direction φ of the incident polarization at λ = 444 nm. They are fitted for each wavelength to $\cos^2\varphi$ and $\sin^2\varphi$ functions respectively. The ratio of axial to transverse scattering $A_{//}(\lambda)/A_{\perp}(\lambda)$ measuring unambiguously the ratio of the MD and EQ contributions to the ED scattering is shown in Fig. S4. It exhibits a sharp maximum of 28% at 450 nm, far higher than any reported value so far [21,23].

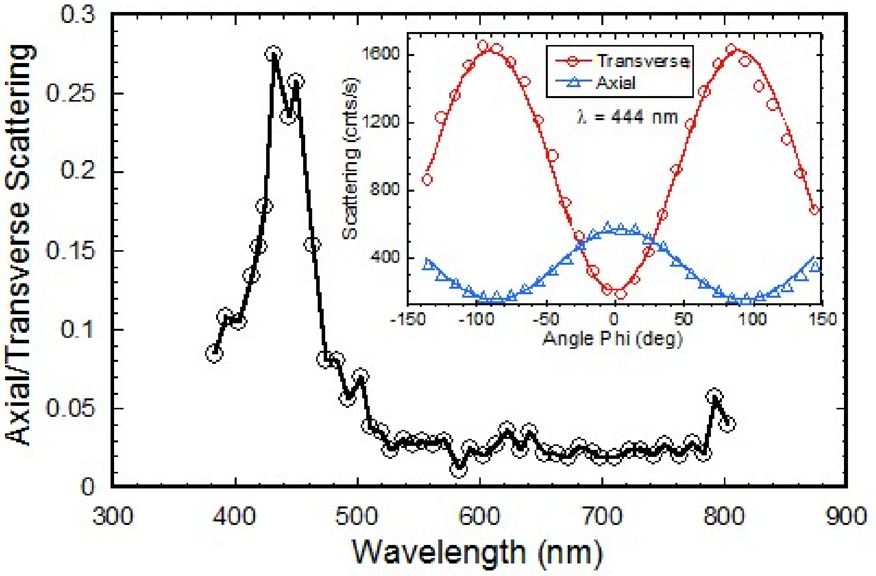

Figure S4: *Ratio of axial to transverse scattering* A_H/A_V *vs wavelength. Inset shows transverse (red) and axial (blue) scattering measured at* λ*=444 nm. Solid lines are fits to* $\sin^2$ *and* $\cos^2$ *functions respectively.*

The MD+EQ and ED contributions are extracted separately by normalizing the data with a reference dispersion of calibrated silica nanoparticles (D_{SiO2} = 96 nm) in water. The scattered intensity from the reference sample is similar to equation (S1a) by replacing $\left|S_1(\theta=90°)\right|^2/k^2$ by $\sigma_{ref\,(\theta\,=\,\varphi\,=\,90°)}$ the differential scattering cross section of a silica particle in water at scattering angles $\theta=\varphi=90°$. The MNC and reference signals were collected in the same experimental conditions so that the quantities I_0, $\delta\Omega$ and $g(\lambda,\delta\Omega)$ are the same for MNCs and reference. Dividing equations (S1a,b) for MNCs by the reference yields the differential scattering cross sections of a MNC along the particular directions (θ,φ):

$$\sigma_{\perp}^{ED}(\theta=\varphi=90°)=\frac{\left|S_1(\theta=90°)\right|^2}{k^2}=K\,\frac{A_{\perp}(\lambda)}{A_{\perp}^{ref}(\lambda)}\,\frac{T_{ref}(\lambda)}{T(\lambda)}\,\sigma_{ref}^{\theta=\varphi=90°}(\lambda) \qquad \text{(S2a)}$$

$$\sigma_{//}^{MD+EQ}(\theta=90°,\varphi=0)=\frac{\left|S_2(\theta=90°)\right|^2}{k^2}=K\,\frac{A_{//}(\lambda)}{A_{\perp}^{ref}(\lambda)}\,\frac{T_{ref}(\lambda)}{T(\lambda)}\,\sigma_{ref}^{\theta=\varphi=90°}(\lambda) \qquad \text{(S2b)}$$

Superscripts ED and MD+EQ remind that $\sigma_\perp$ and $\sigma_{//}$ are respectively dominated by the scattering of the electric dipole and of the added contribution of the magnetic dipole and electric quadrupole. $K = N_{ref} / N_{MNC}$ is a constant independent of wavelength. The scattering cross section of a silica sphere in water in transverse polarization $\sigma_{ref}^{\theta=\varphi=90°}$ is computed by the Mie theory [31]. The transmission of highly dilute suspensions is dominated by the absorbance of the solvent so that the ratio $T_{ref}(\lambda)/T(\lambda)$ is simply 1. The resulting cross sections (equations (S2a,b)) are plotted in Fig. 3a of the article.

5 – Determination of the dielectric function of silver for T-Matrix numerical simulations of the scattering of a MNC:

The literature offers several data sets for the refractive index of silver [S4]. The most two widely used are found in the Palik handbook compilation [S5,S6] and in the paper by Johnson and Christy [S7]. Unfortunately, they are inconsistent making realistic modeling of the performance of silver in optical applications difficult [S4]. In order to use realistic values of the refractive index in our numerical simulations, we checked the two data sets. We measured the optical extinction of a suspension of silver nanoparticles with a UV-visible spectrometer and we simulated the extinction by the Mie theory. It is important to point out that the silver nanoparticles used in this experiment, synthesized by us, are precisely the ones used to synthesize the MNC satellites (diameter = 25 nm). The Mie theory has no mystery and the simulation requires no particular assumption. The data are shown in Fig. S4. Simulations obtained with the Johnson-Christy data set are far from the experiment and should be discarded. The Palik data set gives a much better agreement and could be used as such. We further improved the dielectric function by introducing a small correction explained in equation (S3) below.

$$\varepsilon_{AgCorr} = \varepsilon_{Palik} + \frac{f_{pPalik}^2}{f^2 + if\gamma_{Palik}} - \frac{f_{Corr}^2}{f^2 + if\gamma_{Corr}} \tag{S3}$$

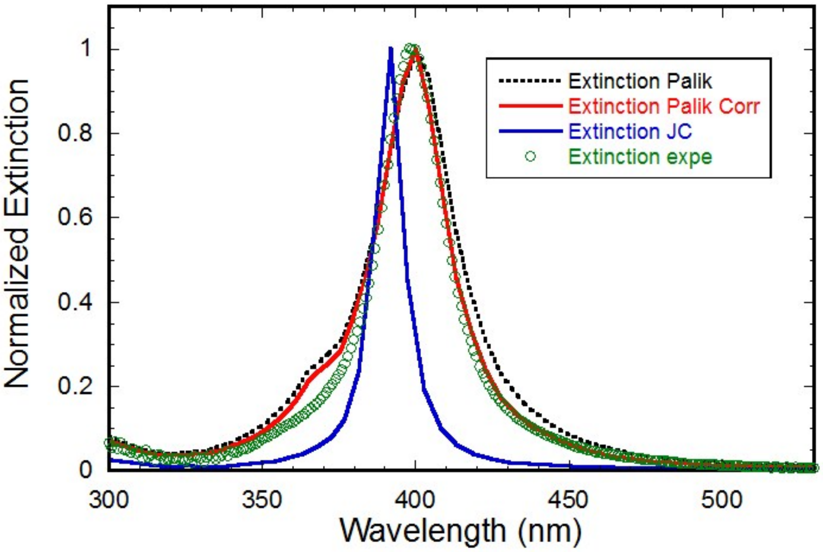

Figure S5: *experimental (green circles) and simulated extinction of a suspension of silver nanoparticles used in this work. Simulations are performed by Mie theory with Johnson-Christy (blue line) Palik (black dashed line) and Palik-corrected (red line) data sets for the refractive index of silver.*

We first fitted the long wavelength region of the Palik data to a Drude model. A perfect fit is obtained with f_{pPalik} = 2121.15 THz and γ_{Palik} = 15.15 THz. We then subtract this Drude component from the permittivity and we add a corrected Drude model with slightly different parameters f_{Corr} = 2131.15 THz and γ_{Corr} = 8.15 THz to obtain an almost perfect agreement, as shown in Fig. S5.

6 – T-Matrix numerical simulation of the scattering of a single MNC:

In order to interpret the scattering data, the electromagnetic response of MNCs was computed numerically by a method introduced in reference 24. The MNCs were first constructed by distributing non-intersecting spherical satellites on the surface of the core sphere of diameter 96 nm. Each satellite was constituted of a silver sphere of diameter 25 nm surrounded by a silica shell of thickness 5 nm. The final state is obtained by defining an effective repulsion energy that is subsequently minimized to evenly distribute the satellites by maximizing the distance between them. In a second step, we employed a T-Matrix code developed by Mackowski [30] to simulate the electromagnetic response of the MNCs. It is a FORTRAN code providing the solution to Maxwell's equations for an ensemble of non-overlapping spheres. Following the formalism of the Mie theory describing the scattering of a single sphere [32], the scattered fields are expanded in series of scattering coefficients a_i^{MNC} and b_i^{MNC} computed for the whole cluster. The first order coefficients a_1^{MNC} and b_1^{MNC} correspond respectively to the electric (ED) and magnetic (MD) dipolar mode of the MNC, a_2^{MNC} to the electric quadrupole radiation (EQ) and so on. The refractive indices of silica [S8], water [S9] and ethanol [S10] were taken from the literature. The dielectric function of silver is determined from UV-visible extinction spectra as described is section 4 above.

The computed transverse and axial scattering cross sections of the MNCs $|S_1|^2/k^2$ and $|S_2|^2/k^2$ are displayed in Fig. 3a. The experimental signals are extremely well reproduced for a number of satellites of 22, consistent with TEM images (Fig. 1b).

7 – Regression model for ellipsometric data

The ellipsometric measurements were performed in the 240–1000 nm wavelength range with a variable-angle spectroscopic Woollam ellipsometer M2000F. The spot size was set to 50 µm which is small enough to ensure that the footprint of the beam is totally included in the sample of width 100 µm.

Fig. S6a shows the spectral evolution of the correlation coefficient of the fit to equation 1. This coefficient may be viewed as a test of how non-local the retrieved electromagnetic parameters are. Fig. S6b-d illustrates situations of good (b,d) and poor (c) linear correlation.

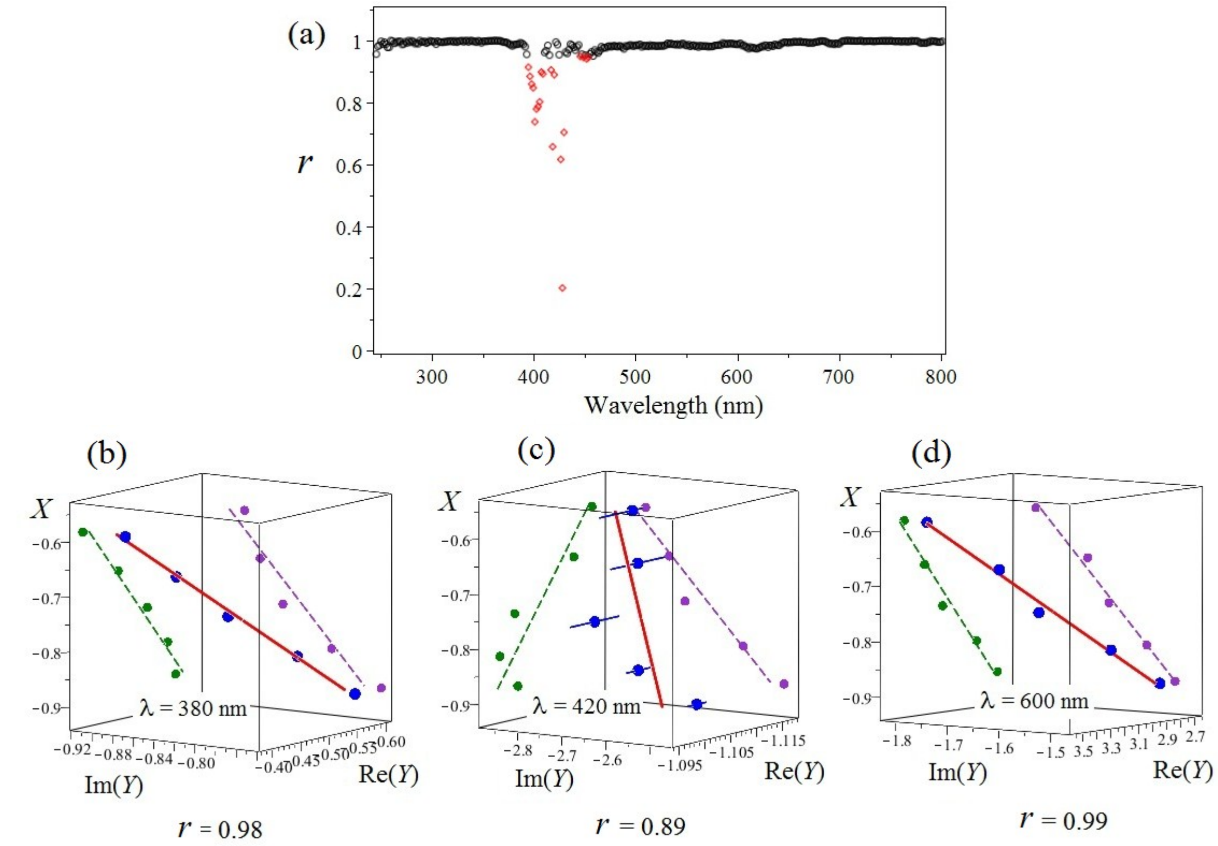

Figure S6: *(a) Linear Pearson correlation coefficient r showing the goodness of fit across the range of visible wavelengths. Data points with r>0.95 (black circles) correspond to symbols in Fig.2 of the article. Red diamonds denote data points with r<0.95. (b-d) Illustration of the linear relationship Y=AX+B (solid line) at three different wavelengths: (b) λ = 380 nm, r = 0.98 (c) λ = 420 nm, r = 0.89 (poor correlation) and (d) λ = 600 nm, r = 0.99. Symbols are experimental data collected at five angles of incidence (50, 55, 60, 65 and 70°). Y, A and B are complex numbers. The projections of the linear regression on the planes (X,Re(Y)) and (X,Im(Y)) are shown (dashed lines).*

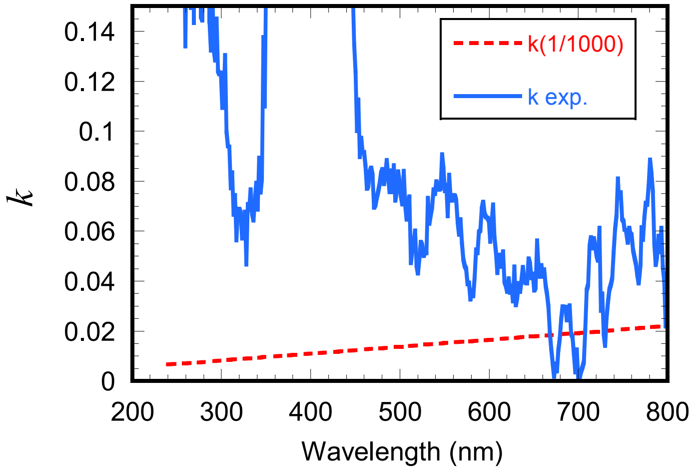

Figure S7: *Check of the validity of a semi-infinite approximation. The solid blue line represents the experimental values of the imaginary part of the refractive index (detail of figure 4b). The red dashed line corresponds to a contribution of the reflection at the bottom interface below 0.1%.*

The consistency of the semi-infinite assumption is checked as follows. A wave reflected at the bottom interface (metamaterial to glass substrate) travels a distance of order $2e$ across the metamaterial of thickness e. Its intensity is reduced by a factor $T = \exp(-4\pi k e/\lambda)$. The red line in figure S7 corresponds to an attenuation T = 1/1000 for a sample of thickness e = 5 µm. The imaginary part of the refractive index of the metamaterial (blue line) is mostly above this line, indicating that the contribution of the reflection at the bottom interface is below 0.1%, except for a few wavelengths in the region 660-700 nm, far from resonance, where the experimental noise precludes a clear conclusion.

8 – Energy balance of the HS

Making sure that the effective HS is indeed dissipative amounts to verifying that the absorption efficiency ($Q_{\text{abs}} = \sigma_{\text{abs}}/S$, where σ_{abs} is the absorption cross-section and S is the geometrical cross-section) is positive. Here we calculate Q_{abs} by two different methods: circles in Fig. S8 represent Q_{abs} computed by calculating the ohmic losses, while the red curve represents Q_{abs} computed by calculating Q_{ext}- Q_{scatt}, where Q_{ext} (resp. Q_{scatt}) is the extinction (resp. scattering) efficiency. According to the optical theorem, these two quantities must be equal. For completeness, we recall the expressions for Q_{ext}, Q_{abs} and Q_{scatt}:

$$Q_{\text{ext}} = -\frac{1}{2SI_0} \oiint_{\Sigma} \text{Re}\left\{\mathbf{E}_{\text{inc}} \times \mathbf{H}^{*}_{\text{scatt}} + \mathbf{E}_{\text{scatt}} \times \mathbf{H}^{*}_{\text{inc}}\right\} \mathbf{n}_{\sigma} d\sigma$$

$$Q_{\text{abs}} = \frac{1}{2SI_0} \iiint \text{Re}\left\{\mathbf{J} \cdot \mathbf{E}\right\} dV$$

$$Q_{\text{scatt}} = \frac{1}{2SI_0} \oiint_{\Sigma} \text{Re}\left\{\mathbf{E}_{\text{scatt}} \times \mathbf{H}^{*}_{\text{scatt}}\right\} \mathbf{n}_{\sigma} d\sigma$$

In the formulas for the efficiencies, I_0 is the incident intensity on the effective particle, $\{\mathbf{E}_{\text{inc}}, \mathbf{H}_{\text{inc}}\}$ ($\{\mathbf{E}_{\text{scatt}},\mathbf{H}_{\text{scatt}}\}$) is the incident (scattered) electromagnetic field, $\mathbf{J}$ is the current density, Σ is a closed surface surrounding the effective particle at an arbitrary distance, $\mathbf{n}_{\sigma}$ is the unit vector normal to Σ, $d\sigma$ is an infinitesimal surface element of Σ and dV is an infinitesimal volume element contained within Σ.

Fig. S8 not only shows that the two quantities are equal but also that both methods give positive results for Q_{abs} demonstrating that the effective particle is indeed dissipative.

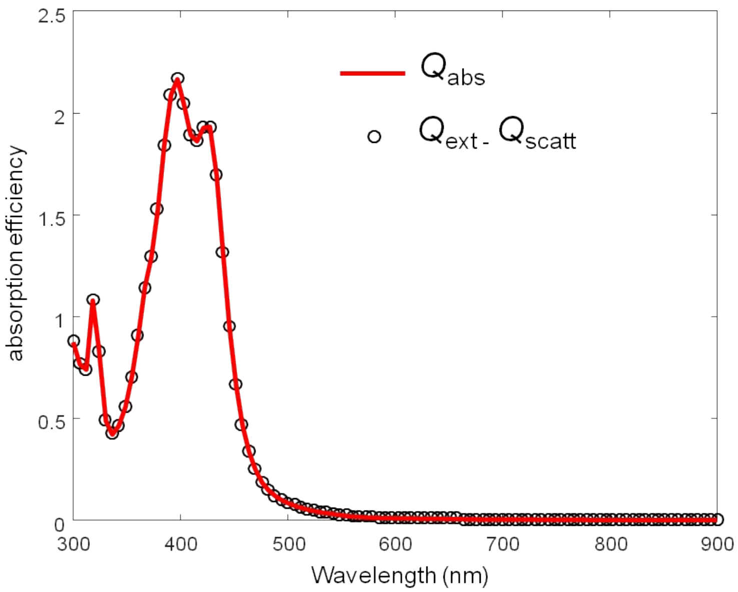

Figure S8: *Absorption efficiency of the HS computed from ohmic losses (circles), while the red curve represents* Q_{abs} *computed by calculating* Q_{ext}- Q_{scatt}, *where* Q_{ext} *(resp.* Q_{scatt}*) is the extinction (resp. scattering) efficiency. It is always positive showing that the HS is dissipative at all wavelengths.*

Additional references for supplementary information:

[S1] Mori, H. *et al.* M. Synthesis of triazole-based amphiphilic block copolymers containing carbazole moiety by RAFT polymerization. *Macromol. Chem. Phys.* **213**, 1803-1814 (2012).

[S2] Katsigiannopoulos, D. *et al.* Nanohybrids based on polymeric ionic liquid prepared from functionalized MWCNTs by modification of anionically synthesized poly(4-vinylpyridine). *J. Polym. Sci. A Polym. Chem.* **50**, 1181-1186 (2012).

[S3] Masse, P. et al. Synthesis of Size-Monodisperse Spherical Ag@SiO2 Nanoparticles and 3-D Assembly Assisted by Microfluidics. *Langmuir,* **29,** 1790-1795 (2013).

[S4] Jiang, Y., Pillai, S. and Green, M. A. Re-evaluation of literature values of silver optical constants. *Opt. Expr.*, **23,** 2133-2144 (2015).

[S5] Palik, E.D. Handbook of Optical Constants of Solids. (Academic Press, London, 1985).

[S6] Winsemius, P., Lengkeek, H. P. and Vankampen, F. F. Structure dependence of optical-properties of Cu, Ag and Au, *J. Phys. F* **79,** 529–546 (1975).

[S7] Johnson, P. B. & Christy, R. W. Optical constants of the noble metals. *Phys. Rev. B* **6,** 4370–4379 (1972).

[S8] Malitson, I. H. Interspecimen Comparison of the Refractive Index of Fused Silica. *J. Opt. Soc. Am.* **55**, 1205-1208 (1965).

[S9] Daimon, M. and Masumura, A. Measurement of the refractive index of distilled water from the near-infrared region to the ultraviolet region. *Appl. Opt.* **46**, 3811-3820 (2007).

[S10] S. Kedenburg, S., Vieweg, M., Gissibl, T. and Giessen, H. Linear refractive index and absorption measurements of nonlinear optical liquids in the visible and near-infrared spectral region, *Opt. Mat. Express* **2**, 1588-1611 (2012).